A&A 674, A220 (2023)
https://doi.org/10.1051/0004-6361/202346100

Astronomy & Astrophysics
Special issue

Solar Orbiter First Results (Nominal Mission Phase)

Langmuir waves associated with magnetic holes in the solar wind

J. J. Boldú[1,2], D. B. Graham[1], M. Morooka[1], M. André[1], Yu. V. Khotyaintsev[1], T. Karlsson[3], J. Souček[4], D. Píša[4], and M. Maksimovic[5]

[1] Swedish Institute of Space Physics (IRF), Uppsala 75121, Sweden
e-mail: jordi.boldu@irfu.se
[2] Department of Physics and Astronomy, Uppsala University, Uppsala 75121, Sweden
[3] Division of Space and Plasma Physics, School of Electrical Engineering and Computer Science, KTH Royal Institute of Technology, Stockholm 11428, Sweden
[4] Institute of Atmospheric Physics of the Czech Academy of Sciences, Bocni II 1401, Prague 141 00, Czech Republic
[5] LESIA, Observatoire de Paris, Université PSL, CNRS, Sorbonne Université, Univ. Paris Diderot, Sorbonne Paris Cité, 5 Place Jules Janssen, 92195 Meudon, France

Received 7 February 2023 / Accepted 12 May 2023

ABSTRACT

Context. Langmuir waves (electrostatic waves near the electron plasma frequency) are often observed in the solar wind and may play a role in the energy dissipation of electrons. The largest amplitude Langmuir waves are typically associated with type II and III solar radio bursts and planetary foreshocks. In addition, Langmuir waves not related to radio bursts occur in the solar wind, but their source is not well understood. Langmuir waves have been observed inside isolated magnetic holes, suggesting that magnetic holes play an important role in the generation of Langmuir waves.
Aims. We provide the statistical distribution of Langmuir waves in the solar wind at different heliocentric distances. In particular, we investigate the relationship between magnetic holes and Langmuir waves. We identify possible source regions of Langmuir waves in the solar wind, other than radio bursts, by analyzing the local plasma conditions.
Methods. We analyzed data from Solar Orbiter's Radio and Plasma Waves (RPW) and Magnetometer (MAG) instruments. We used the triggered electric field snapshots and onboard statistical data (STAT) of the Time Domain Sampler (TDS) of RPW to identify Langmuir waves and investigate their properties. The plasma densities were derived from the spacecraft potential estimated by RPW. The MAG data were used to monitor the background magnetic field and detect magnetic holes, which are defined as regions with an isolated decrease in $|\boldsymbol{B}|$ of 50% or more compared to the background level. The statistical analysis was performed on data from 2020 to 2021, comprising heliocentric distances between 0.5 AU and 1 AU.
Results. We show that 78% of the Langmuir waves in the solar wind not connected to radio bursts occur in regions of local magnetic field depletions, including the regions classified as isolated magnetic holes. We also show that the Langmuir waves occur more frequently inside magnetic holes than in any other region in the solar wind, which indicates that magnetic holes are important source regions of solar wind Langmuir waves. We find that Langmuir waves associated with magnetic holes in the solar wind typically have lower amplitudes than those associated with radio bursts.

Key words. solar wind – plasmas – waves – Sun: heliosphere

1. Introduction

The solar wind is a weakly collisional plasma, where the electron distribution is not significantly altered by Coulomb collisions. As a result, the solar-corona-accelerated electron distribution persists into the interplanetary medium and can be unstable to plasma instabilities. Electron distributions in the solar wind typically consist of a Maxwellian core, a superthermal halo, and a field-aligned strahl directed away from the Sun (Feldman et al. 1975; Phillips et al. 1989; Verscharen et al. 2019). The electron distribution in the solar wind has been observed to evolve with heliocentric distance (McComas et al. 1992; Štverák et al. 2009; Halekas et al. 2022). In particular, it has been found that the strahl dissipates into the halo as the solar wind moves farther from the Sun (Maksimovic et al. 2005). Since collisions can only play a minor role, especially for the nonthermal regions of the distribution, wave–particle interactions are expected to play an important role in the evolution of the electron distribution of the solar wind. Which waves are dominant in this process is still not well understood. A strong candidate is Langmuir waves (LWs) because of their relationship with electrons.

Langmuir waves are electrostatic waves near the electron plasma frequency. The largest amplitude LWs in the solar wind are typically connected with type II (Cairns 1986; Graham & Cairns 2015) and type III (Bardwell & Goldman 1976; Robinson 1992; Pulupa et al. 2020) radio bursts (RBs) associated with coronal mass ejection shocks and solar flares, respectively. In these cases, LWs are generated by electron beams via the bump-on-tail instability. However, a large number of LWs not related to RBs occur in the solar wind (Briand 2015); some of these LWs have been associated with different source regions, such as magnetic reconnection (Huttunen et al. 2007; Vörös et al. 2021) and switchbacks (Rasca et al. 2022). However, the source of most LWs in the solar wind is not fully understood.

Previous observations at 1 AU have shown that LWs in the solar wind often occur inside magnetic holes (MHs; Lin et al. 1995). A MH is typically defined as a region with a magnetic

field magnitude lower by 50% or more with respect to the background magnetic field (Karlsson et al. 2021). Magnetic holes are common in space plasmas, such as in the solar wind and planetary magnetosheaths (Turner et al. 1977; Yao et al. 2017, 2019). These structures have magnetic pressure balanced by the plasma pressure and are often found in the solar wind, with a mean occurrence of ∼3 holes per day in the inner heliosphere (Volwerk et al. 2020). Their origin is still debated, but it has been argued that they could be remnants of mirror modes (Winterhalter et al. 1994). To explain the origin of LWs in MHs, it was suggested that the strahl population entering a MH could develop into a beam distribution via the adiabatic motion of electrons and time-of-flight effects (Briand et al. 2010). Nevertheless, the presence of such a beam inside MHs has not been confirmed. Understanding the relation between MHs and LWs will help characterize the source regions of LWs and provide insight into their role in shaping the solar wind.

The goal of this paper is to identify the LWs in the solar wind that are not related to RBs and statistically provide their properties and occurrence distribution using Solar Orbiter data. We show that LWs are more likely to be found inside MHs. We analyze the properties of MHs that contain LWs, such as depth and size, and characterize the solar wind conditions under which LWs are more common. We also discuss the generation mechanism of LWs inside MHs using high-resolution data from the Magnetospheric Multiscale (MMS) spacecraft.

The outline of this paper is as follows: We describe the data and instruments used in Sect. 2. In Sect. 3.1 we present statistics of the LWs in the solar wind and compare the occurrence of RB-related LWs with that of the non-RB-related LWs. In Sect. 3.2 we investigate which MH properties play a role in the manifestation of LWs. In Sect. 3.3 we perform an analysis of the plasma conditions under which LWs are observed. We present a case study of two MH events using MMS data in Sect. 4 and discuss LW generation mechanisms. The conclusions are stated in Sect. 5.

2. Methods and instrumentation

For the statistical analysis, we investigate electric and magnetic field data from Solar Orbiter over the period 2020–2021. The Radio and Plasma Waves (RPW) instrument suite (Maksimovic et al. 2020), on board Solar Orbiter (Müller et al. 2020), measures the electric field using three 6.5 m antennas in the plane perpendicular to the sunward direction. The analog signals from the three antennas are sampled by the Time Domain Sampler (TDS) receiver (Souček et al. 2021), which is part of the RPW instrument suite.

We use triggered snapshot waveforms (TSWFs) and the onboard statistical data (STAT) products from the TDS receiver. The TSWFs have a typical sampling rate of 262.1 kHz and a duration of approximately 60 ms, so the local electron plasma frequency f_{pe} is well resolved, where the typical f_{pe} values vary between ∼20 kHz at 1 AU and ∼60 kHz at 0.5 AU. The snapshots analyzed here are triggered by the TDS wave detection algorithm (Souček et al. 2021), which selects the most relevant snapshots by applying a quality factor to them. The snapshots are processed every second, and only the ones with the highest quality factor in the queue are downlinked. Typically, the TSWF buffer is emptied every 1−6 h in survey mode and a total of 180 to 360 triggered snapshots are captured per day, with some exceptions where fewer snapshots are obtained (between 40 and 70), especially in the early stages of the mission. An example of a TDS snapshot containing a LW is shown in Fig. 1e.

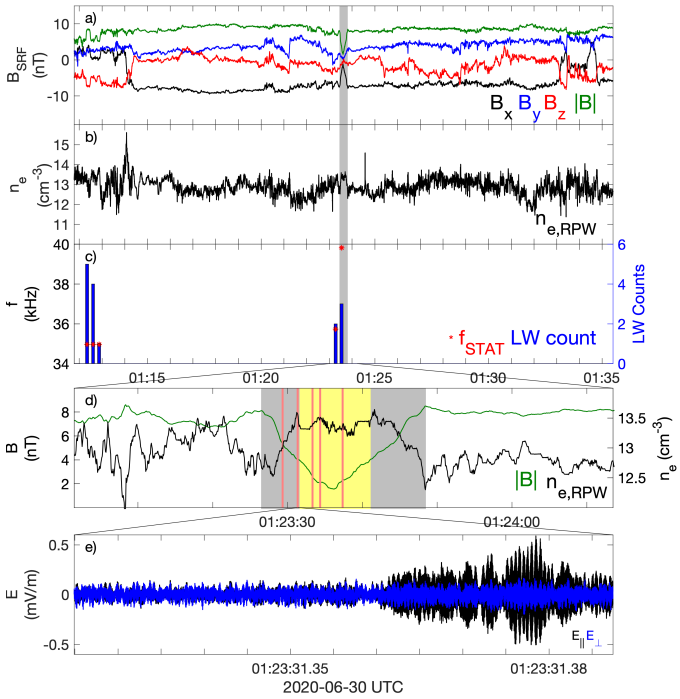

Fig. 1. Overview plot from Solar Orbiter's RPW and MAG instruments around a MH. (a) Magnetic field components in SRF coordinates (black, blue, and red) and the magnetic field magnitude (green) around a MH (gray highlight). (b) Density from the spacecraft's potential around a MH (gray highlight). (c) STAT data from the TDS onboard algorithm around a MH (gray highlight). Each bar indicates a STAT packet with at least one LW. The height of the blue bars (right axis) indicates the number of LWs in the STAT packet, and the red asterisks (left axis) are the median frequency of all the waves in that STAT packet. (d) Zoomed-in view of a MH that contains several LWs (red highlights). The density obtained from the spacecraft (s/c) potential (black) increases as the magnetic field magnitude (green) decreases, indicating that this magnetic structure is in pressure balance. The center of the MH, that is, all points where the magnetic field magnitude is less than half of the background level, is highlighted in yellow, and the MH edges are highlighted in gray. The full MH interval is the combination of the yellow and gray intervals. (e) TDS snapshot of the perpendicular (blue) and parallel (black) electric field components, showing a LW found inside a MH.

To complement the triggered snapshots we use STAT data to provide continuous coverage. An example of STAT data is presented in Fig. 1c. The blue bars indicate LW counts in each data packet, and the median frequency is represented by the red asterisks. The STAT data consists of statistical properties of all the snapshots that contain waves or dust impacts, including those selected for downlink as triggered snapshots as well as those with a lower quality factor that were not chosen for transmission. The disadvantage of the STAT data is that we cannot study individual waveforms but statistical quantities of all LWs detected in a time interval of 16 s. The onboard wave detection algorithm (Souček et al. 2021) classifies snapshots containing waves or dust impacts and computes the median frequency of the detected waves, rms and maximum amplitudes, among other quantities, and the total wave count of each 16 s data packet. Since every snapshot is processed in 1 s, the maximum number of waves a STAT packet can have is 16. For the zoomed-in interval in panel d, there are two STAT packets, with the first one having two LWs and the second one three. In this example, we also

observe in the STAT data several LWs outside the highlighted MH at the beginning of the interval in panel c.

Once we obtained the triggered snapshots and STAT packets, we needed to identify the ones with LWs. To identify LWs with TSWF data, we first applied a fast Fourier transform to the TDS snapshots. We analyzed each snapshot's power spectral density and identified the frequency, $f_{\rm pk}$, at which the power peaks. We identified the waveform as a LW if the peak power, $f_{\rm pk}$, is between 0.5 $f_{\rm pe}$ and 1.5 $f_{\rm pe}$ and if its maximum power is more than two orders of magnitude above the median power in this frequency range. This frequency range is sufficient to capture the observed LWs (Graham et al. 2021). Here, $f_{\rm pe}$ is obtained from the electron density calculated from the spacecraft potential (Khotyaintsev et al. 2021). To avoid spurious peaks that are not related to waves, the power spectral density was smoothed using a 2nd order median filter. Furthermore, we note that because of the antenna plane configuration, LWs with electric fields close to the radial direction will have their amplitude significantly underestimated. To identify LWs in the STAT data, we check that the median frequency $f_{\rm med}$ of a packet is between 0.5 $f_{\rm pe}$ and 1.5 $f_{\rm pe}$. To get the total number of LWs, we add the wave counts in a STAT packet containing LWs.

We manually removed the snapshots and STAT data products with strong interference that impacted the instrument's performance. The periods with the most interference were found between January and March 2021. Moreover, during 2020 and 2021, Solar Orbiter was in the cruise phase, and there were days without TSWF or STAT data or variability in the number of triggered snapshots transmitted.

By inspection of TDS and the Thermal Noise Receiver, which is part of the RPW instrument, we manually identified periods of type III RB activity. All the snapshots containing LWs in those periods are labeled as connected to RBs. Throughout this paper, we refer to LWs in the solar wind that are not connected to RBs as solar wind LWs to differentiate them from those that are RB related LWs.

To measure the background magnetic field $\boldsymbol{B}$ and detect the isolated MHs, we used the Magnetometer (MAG) instrument's data (Horbury et al. 2020). MAG provides 3-axis magnetic field measurements at 8 Hz in the spacecraft reference frame (SRF), where the x-axis points sunward, the negative y-axis is along the ram direction, and the z-axis is along the orbit's normal direction. We used the definition of MHs from Karlsson et al. (2021), where a MH is described as a region of an isolated decrease in $|\boldsymbol{B}|$ of 50% or more from the background. The background level, B_0, was obtained with a 5-min moving-mean window, such that $B_0 = \text{mean}(|B|)_{5\,\text{min}}$, and it was then subtracted from the original signal, $|B|$. The difference $\Delta B = |B| - B_0$ was normalized by B_0 to calculate the relative magnetic depression. To avoid high-frequency variations, the result was smoothed by a 1 s moving-mean. This process is expressed as

$$\Delta B/B_0 = \text{mean}\left(\frac{|B| - B_0}{B_0}\right)_{1\,\text{s}}, \tag{1}$$

where the first and last points meeting the condition $\frac{\Delta B}{B_0} < 0.5$ are the start and end points of the MH central region, as shown by the yellow interval in Fig. 1c. We can define the edges of the MH to be the closest peaks above B_0 before and after the MH central region, highlighted in gray Fig. 1c. In this way, the full MH interval consists of the MH center (yellow area) and the MH edges (gray area). Only the deepest depression within two minutes satisfying $\frac{\Delta B}{B_0} < 0.5$ is identified as a MH, hence the name isolated MHs.

Table 1. Number of LWs identified with TSWFs and STAT.

Source	TSWF	STAT
Radio bursts	889	7929
Solar wind	2263	4107
MH	182	153
Total	3334	13 387

An example of a MH containing LWs captured by STAT and TSWFs is shown in Fig. 1. Overviews of the solar wind magnetic field and density are presented in panels a and b, where the isolated MH, highlighted in gray, is surrounded by rather quiet solar wind conditions. Panel d shows a zoomed-in view of the isolated MH, where the full MH interval is highlighted in gray and the yellow interval is the region between the first and last points meeting the conditions in Eq. (2) (i.e., where $\frac{\Delta B}{B_0} < 0.5$). Depletion of the magnetic field intensity associated with the density enhancement that can maintain the plasma and magnetic pressure balance has been observed. This is a typical characteristic of the MHs (Winterhalter et al. 1994; Madanian et al. 2020). We observe five triggered snapshots containing LWs at the times indicated by the vertical red lines. In panel e we plot the measured high-resolution electric field waveform of the second sampled LW during this event. The snapshot shows the two components of the measured electric field, where $E_\perp$ (blue) is perpendicular to the magnetic field and $E_\parallel$ (black) is the electric field component aligned with the projection of $\boldsymbol{B}$ in the antenna plane. For this snapshot, we find that $E_\parallel \gg E_\perp$, which is expected for LWs.

3. Results

3.1. Statistical characteristics of Langmuir waves

In this section we characterize some of the solar wind LWs and identify possible sources, paying special attention to those occurring at MHs. We obtain two data sets of LWs from the triggered snapshots and STAT data. We divided each of these data sets into different source regions: RB regions, solar wind regions (excluding RB times), and MH regions (which are a subset of the solar wind regions). For this study, we look at data between 2020 and 2021, which includes three perihelia at around 0.5 AU. The results are shown in Table 1. For the TSWF data set, 27% of waves are connected to type III RBs regions and 73% are solar wind LWs. From this 73% of LWs, around 8% are inside the full MH intervals. A total of 1617 isolated MH were identified, which corresponds to an average of about 3 per day. Solar Orbiter dwells inside MHs less than 0.1% of the time. Thus, 8% of the triggered LWs in the solar wind occur in less than 0.1% of the time, suggesting a relation between MH and LW in the solar wind.

With STAT data, the fraction of waves inside MHs in the solar wind is reduced to 4%, but it is still high enough to suggest that there is indeed a correlation. In regions with high LW activity, such as RB regions, many snapshots with LWs are obtained and the TSWF buffer is filled in quickly and not all the snapshots can be transmitted (only the ones with the highest quality factor) whereas with STAT more events can be sent in the form of statistical averages. This explains the difference between both data sets in Table 1. It is also possible that LWs with very low amplitudes do not meet the thresholds set in the onboard algorithm, which are fixed and configured via telecommand

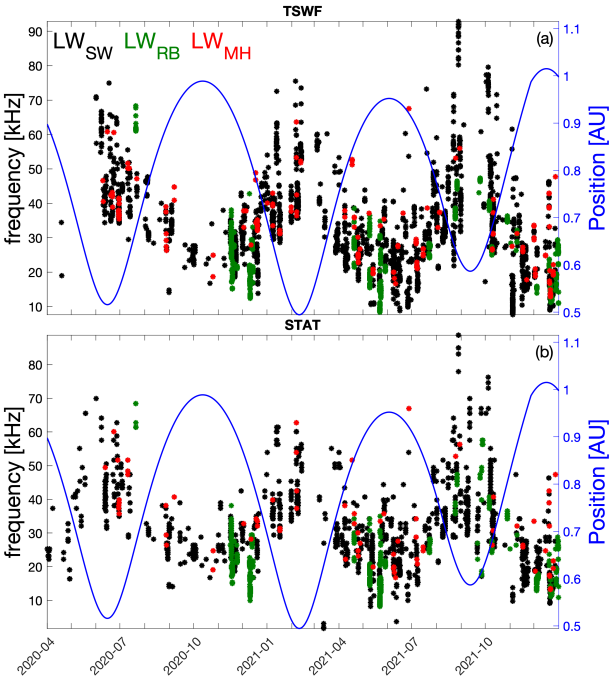

Fig. 2. Distribution of LWs throughout Solar Orbiter's trajectory observed by the RPW/TDS instrument. (a) TSWF data. Shown are the frequency of all triggered snapshots containing LWs captured between 2020 and 2021 (black), LWs associated with MHs (red), and LWs associated with RB source regions (green). Each circle represents a triggered snapshot that contains a LW. Solar Orbiter's distance from the Sun is plotted for reference on the right axis (blue line). (b) STAT data. Shown are the median frequency of all STAT data packets containing LWs captured between 2020 and 2021 (black), data packets containing LWs associated with MHs (red), and data packets containing LWs associated with RB source regions (green). Each circle represents a data packet that contains between 1 and 16 LWs. Solar Orbiter's distance from the Sun is plotted for reference on the right axis (blue line).

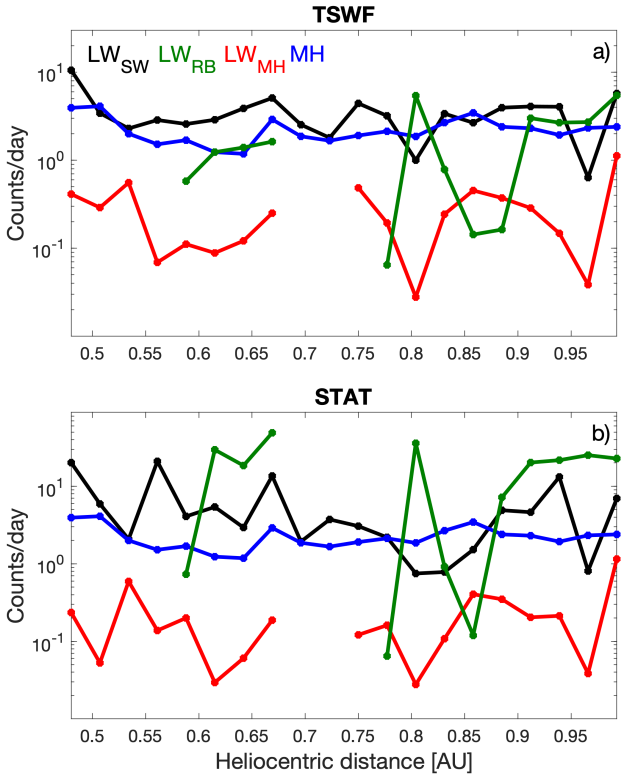

Fig. 3. Radial distribution of LW and MH counts per day. (a) Data from TSWFs. Shown are the radial distribution of the occurrence of the solar wind LWs (black), RB LWs (green), the MH LW (red), and MHs (blue). (b) Data from the STAT product. Shown are the radial distribution of the occurrence of the solar wind LWs (black), RB LWs (green), the MH LW (red), and MHs (blue).

(Souček et al. 2021). These snapshots are, therefore, not classified as waves. This is especially the case for the waves associated with MHs, which are typically of low amplitude, as we show later in this section.

The distribution of the identified LWs is shown in Fig. 2. Panel a corresponds to triggered snapshots with their peak frequency indicated on the left axis. Similarly, panel b shows STAT data packets containing 1 to 16 LWs, and the frequency indicated in the left axis is the median frequency of all the waves inside that packet. Different categories of LWs are also indicated by different colors with green for those related to RBs, red for the ones inside MHs and black for the rest of solar wind LWs. The frequency of the waves is anticorrelated to the distance. This is as expected since the frequency is proportional to density, which decreases with distance from the Sun. For both TSWFs and STAT, the LWs related to RBs appear as clusters of several snapshots and are associated with high solar activity. In contrast, LWs in the solar wind and inside MHs are found more consistently throughout the spacecraft's trajectory.

Next, we investigated how LWs and how their correlation with MHs depends on heliocentric distance. In Fig. 3, we plot the counts per day of LWs at different distances from the Sun from triggered snapshots (panel a) and from STAT (panel b). We observe that the occurrence of LWs associated with MHs is not constant at different radial distances from the Sun. This variability is likely due to variations in LW detection along the orbits, which can be partly instrumental and not necessarily related to MHs occurrence. Overall, there is no dependence on the number of solar wind LWs and MHs with radial distance for those covered with Solar Orbiter so far. The number of MHs per day is almost constant at these distances, making it hard to assess how the presence of LWs varies with MHs occurrence. From Fig. 3, we conclude that there are no clear statistical trends of LWs with radial distance with the caveats of data acquisition during the commissioning phase of the Solar Orbiter mission mentioned in Sect. 2.

We now characterize the LWs related to MHs and compare their properties with those in the solar wind and related to RBs. In Fig. 4a, we show the distribution of the maximum amplitude ($E_{\max}$) of LWs using TSWFs. It is not surprising that the LWs connected to RBs dominate in regions of higher amplitude, while the solar wind LWs dominate at lower amplitudes, with a breakpoint between the two at around 2.3 mV m^{-1}. Moreover, the LWs inside MHs have a similar distribution to the rest of the solar wind LWs, but with fewer overall counts. Because of the typical low-amplitude nature of LWs associated with MH, the absence of snapshots containing LWs inside the MHs does not necessarily mean that there is no LW activity happening. It might be the case that the waves have amplitudes below our detection threshold. The plot in Fig. 4b shows the STAT maximum wave amplitude distribution, exhibiting a similar pattern as the one shown with TSWFs. However, the main difference between the two data sets is that the RB-related LWs have higher counts at low amplitudes since we now have information on the snapshots not transmitted as triggered ones, typically the ones of

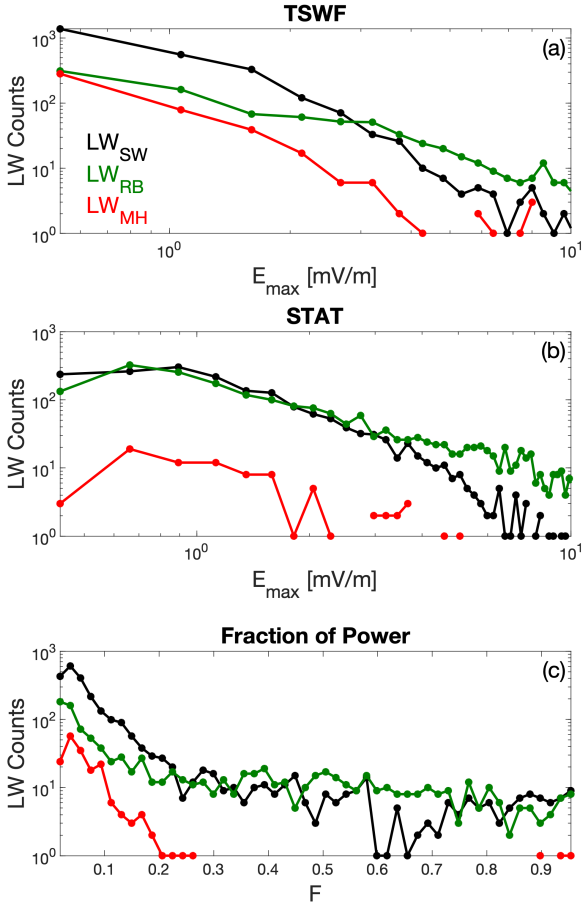

Fig. 4. Amplitudes and fraction of power of LWs in the solar wind associated with different source regions. (a) TSWF data of the maximum amplitude (E_{max}) of solar wind LWs (black), LWs associated with RBs (green), and LWs associated with MHs (red). E_{max} corresponds to the highest electric field measurement value of a snapshot. (b) STAT data of the maximum amplitude (E_{max}) of solar wind LWs (black), LWs associated with RBs (green), and LWs associated with MHs (red). E_{max} corresponds to the highest amplitude of all the snapshots containing LWs in a STAT packet. (c) Fraction of power of the TSWF solar wind LW (black), RB LWs (green), and MH LWs (red).

the lowest amplitude. Despite this increase in low amplitude RB LWs, their distribution is still close to the solar wind LWs at low amplitudes. At an amplitude of approximately 1.5 mV m^{-1} the distributions begin to differ, with the RB dominating at higher amplitudes.

Next, we investigated the polarization of the wave electric field. For this, we calculated the fraction, F, of the perpendicular electric field power to the total electric field power (Malaspina et al. 2011):

$$F = \frac{\Sigma E_{\perp}^2}{\Sigma(E_{\perp}^2 + E_{\parallel}^2)}. \quad (2)$$

The fraction of power is shown in Fig. 4c. Looking at the solar wind LWs, we observe waveforms with $E_{\parallel} > E_{\perp}$, and a similar trend is followed by the waves associated with MHs. The majority of the solar wind LWs, including the ones related to MHs, are close to being field-aligned, indicating LW activity rather than Z-mode waves or upper hybrid waves (Graham & Cairns 2013). For RB LWs, a significantly larger proportion of waves have intermediate values of F, which were interpreted as a combination of Langmuir and Z-mode waves (Malaspina et al. 2011; Graham & Cairns 2013). We note that when the magnetic field is close to the radial direction, $E_{\parallel}$ is not well determined, thus producing an overestimation of F, which explains the LWs with high F inside MHs.

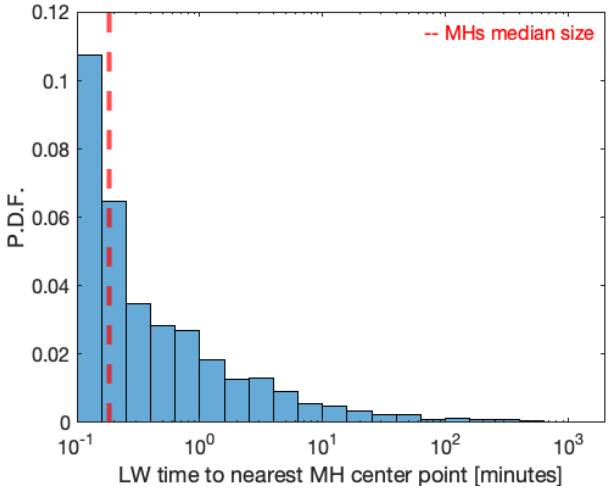

Fig. 5. PDF of the time between LWs and the nearest MH center point. The PDF shows how far from MHs the LWs occur. The histogram shows LW counts normalized by the size of the bin and total counts. The time is taken from the start of a LW to the nearest MH center point. In the vicinity of MHs, most of the LWs occur inside the holes, which corresponds to the first two bins. The median size of the MHs is indicated by the vertical dashed red line.

3.2. Properties of magnetic holes containing Langmuir waves

In this section we compare the probability of finding LWs inside isolated MHs with the probability of finding them in any other region of space in the solar wind. We also investigate whether the MH properties affect the occurrence of LWs.

Figure 5 shows the probability distribution function (PDF) of the time from the triggered LW snapshots to the center point of the nearest MH. The typical temporal width of a MH in the solar wind is between a few seconds and around a minute (Sperveslage et al. 2000; Volwerk et al. 2020). The first two bins of Fig. 5 contain almost only LWs inside MHs. Even though most of the waves are located outside MHs, the probability of finding a LW inside a MH is higher than finding it in any other given region of comparable size with the size of a MH. The observed PDF cannot be reproduced for LWs occurring at random times with respect to the MHs, indicating that MHs are important source regions for solar wind LWs.

We found that 9.1% of the observed isolated MHs have associated LWs. We, therefore, investigate which MH characteristics are suitable for LW generation by comparing the properties of all MHs with those containing LWs. The results of six different properties are shown in Fig. 6. Panel a shows the depth of all the MHs and the MHs containing LWs. The depth ΔB is calculated from the maximum magnetic field value in the MH interval to the minimum. Similarly, panel b shows the normalized depth, which is the depth divided by the background magnetic field. We see that most of the holes have depths of less than 10 nT. From the normalized depth, we observe a less steep decrease in counts toward larger $\Delta B/B_0$ for both distributions, and the proportion of MHs with LWs is bigger for larger $\Delta B/B_0$. However, the low counts make it hard to conclude that MHs of bigger $\Delta B/B_0$ are preferred for the excitation of LWs.

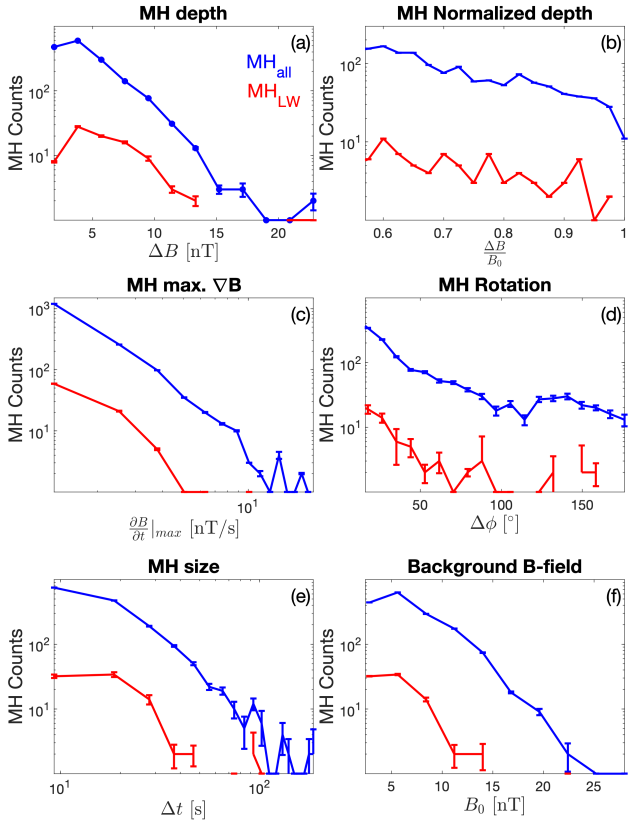

Fig. 6. Histograms of different properties of all isolated MHs found in 2020 and 2021 with Solar Orbiter (blue) and MHs with LWs (red). (a) MH depth calculated as $\Delta B = B_0 - |B|$. (b) MH depth normalized by the background level, $\Delta B/B_0$. (c) Maximum absolute magnetic field gradient inside the MH. The magnetic field gradient is taken by differentiating $|B|$ with respect to time. (d) MH rotation, taken as the angle between the magnetic field vectors after and before the MH. (e) Size in seconds of MHs, calculated from the time of the last point of the MH minus the first point of the MH. (f) Background level of the magnetic field in the five-minute interval where the MH was identified. The error bars are obtained assuming a Poisson distribution that describes the statistics in each bin and are defined as $\delta f/f = 1/\sqrt{N}$, where N is the number of counts in a bin.

Next, we introduce the gradient of the magnetic field $\partial B/\partial t$ by differentiating the time series and taking the result as a proxy of the spatial gradient of $|\boldsymbol{B}|$. The gradient is calculated continuously for every MH, and its maximum value is plotted in Fig. 6c. We observe that the number of MHs with LWs does not exhibit a clear dependence on magnetic field gradients.

Panel d shows the rotation ϕ of the magnetic field after the hole with respect to the direction before the hole. There is no clear preference for LWs occurring at holes of a certain rotation, but there are more likely to occur inside linear holes ($\phi < 25°$) because they are more commonly observed. There is also an increase in the number of MHs at rotations of $\phi \sim 120°$, which are close to the MHs defined as super rotational holes ($\phi \gtrsim 140°$) by Karlsson et al. (2021), but very few LWs have been detected inside these holes.

We plot MH sizes and background B fields in panels e and f, respectively. There is no clear evidence that LWs are more likely to occur when the holes are larger or if they occur when the background field is higher. In summary, the occurrence of LWs in MHs does not show any clear dependence on the MH properties.

3.3. Plasma conditions near solar wind Langmuir waves

We have shown that MHs are LW source regions; however, they only account for a fraction of the total solar wind LWs. In order to identify possible additional sources for LW generation, we now look at all the solar wind LWs and analyze the plasma conditions around them. First, we investigate if the LWs in the solar wind are related to magnetic field depressions more generally. To calculate the local magnetic field depression, we divided the magnetic field at the time of the LWs, $B_{\rm LW}$, by the average $|\boldsymbol{B}|$ over a five-minute interval centered on the starting time of the snapshot B_0. Figure 7a shows the histogram of $B_{\rm LW}/B_0$ for all triggered snapshots containing LWs. We find that solar wind LWs are significantly more common in magnetic field depressions. In particular, we find that 78% of LWs occur for $B_{\rm LW}/B_0 < 1$. We observe a plateau of LW counts starting at ~0.7 $|B_{\rm LW}|/B_0$. About 10% of LWs occur for $B_{\rm LW}/B_0$, similar to the results obtained in Sect. 3.1 where ~8% of LWs were associated with isolated MHs. We note that, besides isolated MHs, the LWs counts corresponding to 0.5 and smaller values of $|B_{\rm LW}|/B_0$ also include MHs that are closer than 2 min to each other.

We compared these results with the general conditions of the magnetic field at all times when we have MAG measurements. To get the background distribution of local conditions $B_{\rm Local}$, we performed a similar analysis with five-minute-spaced points, regardless of the presence of LWs. This distribution is plotted in Fig. 7a. We observe that $|\boldsymbol{B}|$ depressions are as common as $|\boldsymbol{B}|$ peaks, with 48% of the points found in regions of $B_{\rm Local}/B_0 < 1$. The background solar wind conditions of $B_{\rm Local}/B_0 < 0.5$ account only for ~0.1% of the distribution, highlighting the importance of MHs for LW generation in the solar wind.

In Fig. 7b we show the histogram of density perturbations using the same definition as for $\boldsymbol{B}$. We observe that 72% of waves occur at density enhancements, while for typical solar wind conditions density enhancements and depletion regions are equally likely with 47% of the points located in $n_{\rm e,Local}/n_{\rm e,0} > 1$. The increase in LW counts in density enhancements and $\boldsymbol{B}$ depletions suggests the LWs tend to form in pressured balanced structures.

We next investigated if LWs occur close to the largest local depressions of $|\boldsymbol{B}|$. Using the same interval length as before, we looked for the lowest value of $|\boldsymbol{B}|$ and calculated the time difference with the time of the LWs. The results are plotted in black in Fig. 7c, where a clear peak in counts occurs at Time = 0 s. This indicates that a large fraction of the LWs occur at or close to the largest local $|\boldsymbol{B}|$ minimum.

Another property we analyzed is the $|\boldsymbol{B}|$ gradient. We extracted the largest gradient in the interval and calculated how far in time it occurs relative to the LWs time. The histogram is plotted in red in Fig. 7c. We observe a peak at Time = 0 s, although smaller than the one for $|\boldsymbol{B}|$. The presence of LWs close to magnetic field gradients might be an indicator of their relation with regions of enhanced currents. This relation has previously been shown and related to solar wind turbulence rather than isolated current structures (Graham et al. 2021). From Fig. 7c we conclude that LWs tend to occur close to local magnetic field depressions or gradients, indicating the importance of magnetic structures in generating LWs.

4. Discussion

We have found that LWs are more likely to occur in magnetic field depressions. Furthermore, from the LWs occurring in regions ±2.5 min from the MH center points, ~60% are found

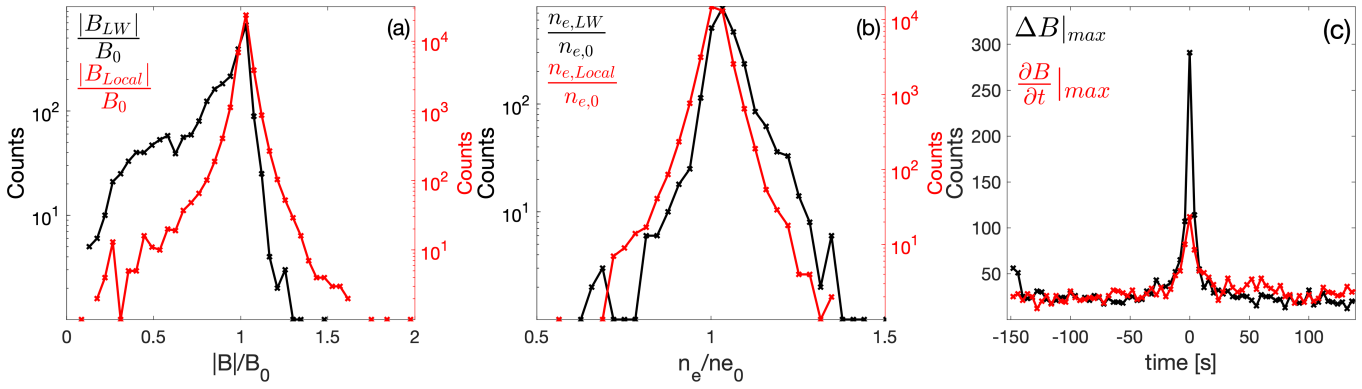

Fig. 7. Plasma conditions near LWs. (a) Ratio between the magnetic field magnitude at the locations of LWs and the background value, B_0, over a five-minute interval (black). The ratio between the magnetic field magnitude at the center of five-minute intervals through all Solar Orbiter's MAG data and the background value, B_0, over the same interval is plotted for reference (red). (b) Ratio between the electron density at the locations of LWs and the background value, $n_{e,0}$, over a five-minute interval (black). The ratio between electron density at the center of five-minute intervals through all Solar Orbiter's MAG data and the background value, $n_{e,0}$, over the same interval is plotted for reference (red). (c) Histogram of time from a LW to the largest magnetic field depression in a five-minute interval with center at the LW (black) and time from a LW to the largest magnetic field gradient (red). Time 0 means that the largest magnetic field depression (or gradient) in an interval ±2.5 min from a LW is at the location of the LW in question.

inside the holes. This is a strong indication that the LWs are excited locally inside these magnetic structures. The local formation of LWs inside MHs was previously observed, using measurements at 1 AU (Briand et al. 2010). Now, we have statistically demonstrated their local formation at different heliocentric distances. In fact, the LWs that are found inside the MHs must have been generated locally due to the density changes associated with the MHs, as LWs cannot propagate at frequencies below ω_{pe}. Langmuir waves generated inside the MHs will be damped when they propagate out of the MHs, due to the increase in wave number as the waves propagate to lower density regions. Similarly, density enhancements inside the MHs will cause reflection of the LWs generated outside the holes and prohibit them from propagating into the holes.

Since the LWs found in MHs must have been generated locally, we proceed to discuss possible instabilities that can arise inside MHs and lead to LWs. Langmuir waves are expected to be driven by the plasma-beam or bump-on-tail instability (Verscharen et al. 2019). It was speculated that the presence of a MH could cause two counter streaming beams in the electron distribution (MacDowall et al. 2008), but this bimodal feature has not been found in observations. Briand et al. (2010) proposed that the strahl population entering the hole could be responsible for the formation of a beam. The strahl is a field-aligned beam population of electrons, commonly found in the solar wind, with energy above ∼50 eV (Gosling et al. 1987). It has been shown that the strahl is focused along $\boldsymbol{B}$ in the inner heliosphere (Berčič et al. 2019; Owen et al. 2022), and broadens around 1 AU (Hammond et al. 1996) before getting completely scattered (Graham et al. 2017). If the strahl is the driver needed for the generation of LWs, this might suggest a radial dependence on the formation of LWs in magnetic field depressions. However, this is not clear from our observations.

To understand the generation mechanisms of LWs inside MHs, we need to look at the electron distribution functions inside the MHs and their surroundings. Measurements at the time of previous studies of LWs inside MHs in the solar wind did not allow for a detailed analysis at electron scales due to the resolution constraints of the instruments. Therefore, we use high-resolution data from the MMS spacecraft (Burch et al. 2016). In burst mode, the MMS spacecraft measure the three-dimensional electron distributions every 30 ms (Pollock et al. 2016). We look for any presence of beam-like features or plateaus in the distribution functions that might explain the presence of LWs inside MHs.

Two MH events were selected during MMS passage in the solar wind on 22 February 2022. Both MHs were observed outside the electron foreshock, meaning the solar wind magnetic field was not connected to Earth's bow shock. Both events were captured in burst mode, and both are linear MHs of approximately 10 s long. The MHs are shown with their respective density increase in Figs. 8a and e. Several LW trains are observed inside the MH on the left Fig. 8b, while the other does not show clear wave activity, besides sections of very low amplitude waves at the end of the hole Fig. 8f. The MHs have a strong influence on the temperature anisotropy; the electron distribution becomes more isotropic when entering the hole, where a decrease in parallel temperature and an increase in perpendicular temperature are observed (not shown). This is similar to previous observations at 1 AU using Cluster data (Briand et al. 2010). From the pitch angle distributions in panels d and h, we see that the solar wind has a clear strahl component (increased flux at pitch angle ∼0°), except in the center of the MHs. The decrease in the flux of the strahl electrons is much more pronounced in the MH that contains LWs, where a clear strahl is no longer observable. On the other hand, the MH with no LWs is not as efficient in scattering the strahl as it still exists inside the MH.

Electron distributions outside and inside the MHs taken from the reduced distributions are shown in Figs. 8c and g. We see the strahl population as an enhancement in phase space density in the $v_{\parallel}$ direction before the hole at parallel velocities between 5000 and 10 000 km s^{-1}, corresponding to energies between 50 and 400 eV in both cases. At the moment of the LWs at ∼01:35:54:700 UTC a relaxation of the distribution occurs, where the $v_{\parallel}$ decreases and the distributions become more isotropic. At this moment, the strahl becomes imperceptible, as shown in Fig. 8d. The same effect is observed in the MH without LWs but to a lesser extent Fig. 8h. Finally, after the MH, the strahl is present again, and the flux at pitch angle ∼90° is slightly enhanced.

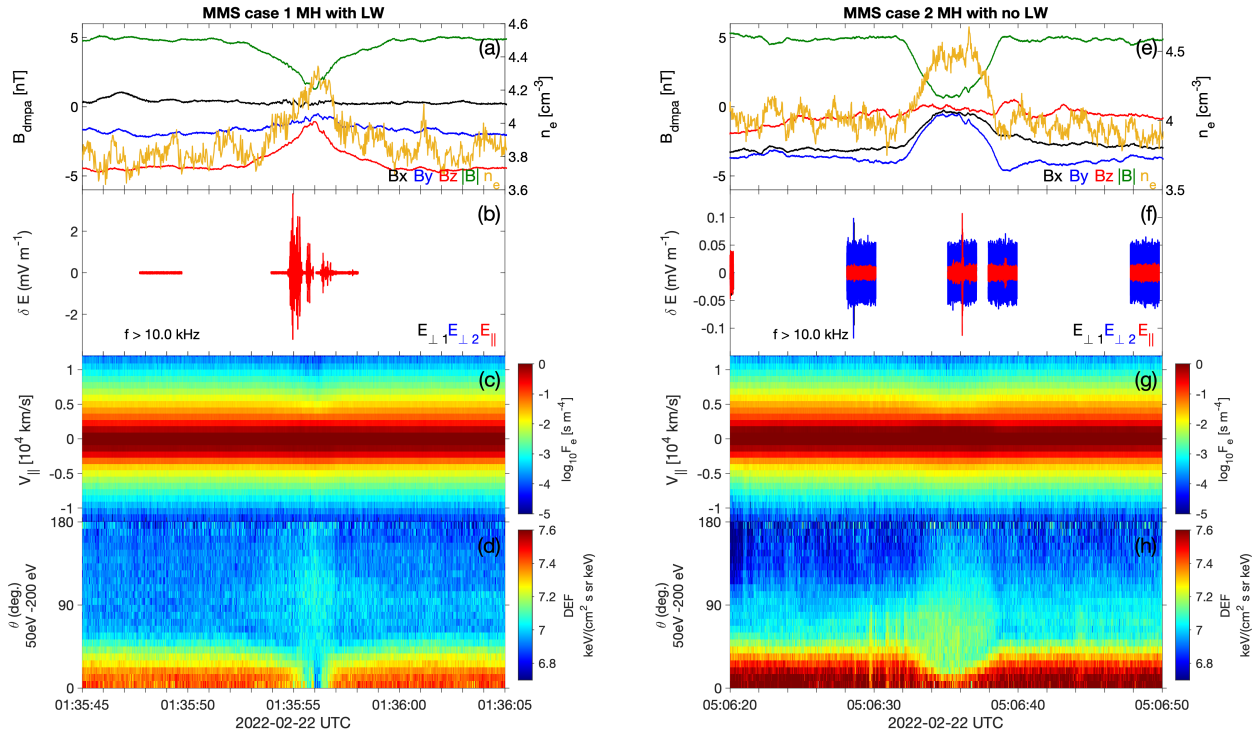

Fig. 8. MMS data of two events with MHs in the solar wind. The left panels show a MH with LW activity, and the right panels show MH without LW activity. (a and e) Magnetic field components (black, blue, and red) and magnitude (green) in the solar wind around a MH, with the density plotted on the right axis. (b and f) High-resolution electric field, showing LW activity in the MH on the left and little to no LW activity in the MH to the right. (c and g) Reduced electron distribution function around a MH. The velocity component parallel to the magnetic field is on the *y*-axis. (d and h) Pitch angle distribution at energies close to the strahl component (50−200 eV). The MH with LW activity shows more strahl scattering than the MH without LW activity.

From the reduced electron distribution functions, we do not observe any beam-like signature or plateaus. This is indeed puzzling because the plasma-beam instability is one of the strongest candidates for triggering LWs; the proposed theory requires a localized positive slope in the distribution function. It has been theorized that the adiabatic motion of strahl electrons combined with a time-of-flight effects would produce the necessary conditions for the formation of a beam inside a MH (MacDowall et al. 2008; Briand et al. 2010). We would expect to find a beam in the distribution function at velocities several times the thermal speed of the core population to trigger LW activity. At this time the Fast Plasma Investigation instrument on board MMS measured electrons up to approximately 1 keV, which should be sufficient to resolve the energy that a weak beam would need to trigger LWs. However, if the density of beams is low, they may not be detected by MMS. For type III RBs near 1 AU the ratio between the beam and core electron densities is typically very small, between 10^{-6} and 10^{-4} (Lin 1990). Therefore, it may be that the beams inside MHs, if present, are not being detected with MMS as they would be less dense or slower than in type III source regions as there is less free energy and lower amplitude waves.

We confirmed, using MMS data, the isotropization of electrons inside MHs in the solar wind and strahl pitch angle scattering as reported previously with Cluster observations. From the two cases we studied, when there was a larger decrease in the high-energy tail of the distribution parallel to $\boldsymbol{B}$, more noticeable LW activity was present. Nevertheless, this isotropization should not produce any beam or shoulder in the parallel velocity electron distribution. On the contrary, it would mitigate any beam-like feature. Until now, the bump-on-tail instability has been the strongest candidate for LW triggering. However, it is not clear what would cause the necessary beams for this instability to occur. In fact, the lack of clear electron beams inside the MHs gives rise to the question of what instabilities are responsible for LW excitation.

5. Conclusions

We have statistically characterized the LWs in the solar wind observed by Solar Orbiter at heliocentric distances between 0.5 AU and 1 AU. The main results are:

1. We observed that ∼8% of the solar wind LWs are associated with MHs, magnetic field depressions with magnitudes of less than half that of the background magnetic field magnitude. This does not include LWs connected to RB regions. Considering that Solar Orbiter spends less than 0.1% of its time inside MHs, LWs are much more common inside MHs than expected from a random generation of waves in the solar wind.
2. More generally, LW excitation is preferred in regions with localized magnetic field depressions, with 78% of the solar wind LWs occurring where the local B field is lower than the background B field. Moreover, 72% of the LWs occur in regions where the density is higher than the background density. This suggests that solar wind LWs are more likely to occur within structures that are in pressure balance.
3. Langmuir waves associated with MHs are typically of low amplitude, with the majority being lower than 1 mV m^{-1}.
4. Despite MHs and LWs being correlated, the presence of the former does not guarantee the latter, as most of the holes do not show any evidence of waves. Nevertheless, when a MH and an external driver (probably a strahl component in the

electron distribution) combine, LW excitation readily occurs. This is shown by the apparent lack of preference toward MHs with specific properties.

The statistics of these results will be improved as more Solar Orbiter data become available. Furthermore, the future availability of data from the Electron Analyzer System of the Solar Wind Analyzer instrument on board Solar Orbiter will make it possible to characterize the relation between the strahl population and MHs with LWs in the solar wind at different distances from the Sun. Investigation of this relation will provide valuable information that will help us determine how LWs are generated inside MHs.

Basing our analysis on previous work regarding LWs observed inside MHs in the solar wind (Lin et al. 1995; MacDowall et al. 2008; Briand et al. 2010), we used the Solar Orbiter spacecraft to provide new quantitative information, and we present evidence that solar wind LWs are correlated with magnetic field depressions. Additionally, we have identified and quantified LWs connected to MHs and RB source regions. These results will help us understand the role that LWs play in the evolution of electron populations in the weakly collisional solar wind.

Acknowledgements. We thank the Solar Orbiter team and instrument PIs for data access and support. J.S. and D.P. acknowledge the support of grant 22-10775S of the Czech Science Foundation. Solar Orbiter data are available at `http://soar.esac.esa.int/soar/#home`.

References

Bardwell, S., & Goldman, M. V. 1976, ApJ, 209, 912
Berčič, L., Maksimović, M., Landi, S., & Matteini, L. 2019, MNRAS, 486, 3404
Briand, C. 2015, J. Plasma Phys., 81, 325810204
Briand, C., Soucek, J., Henri, P., & Mangeney, A. 2010, J. Geophys. Res.: Space Phys., 115, A12113
Burch, J. L., Moore, T. E., Torbert, R. B., & Giles, B. L. 2016, Space Sci. Rev., 199, 5
Cairns, I. H. 1986, PASA, 6, 444
Feldman, W. C., Asbridge, J. R., Bame, S. J., Montgomery, M. D., & Gary, S. P. 1975, J. Geophys. Res., 80, 4181
Gosling, J. T., Baker, D. N., Bame, S. J., et al. 1987, J. Geophys. Res., 92, 8519
Graham, D. B., & Cairns, I. H. 2013, J. Geophys. Res.: Space Phys., 118, 3968
Graham, D. B., & Cairns, I. H. 2015, J. Geophys. Res.: Space Phys., 120, 4126
Graham, G. A., Rae, I. J., Owen, C. J., et al. 2017, J. Geophys. Res.: Space Phys., 122, 3858
Graham, D. B., Khotyaintsev, Y. V., Vaivads, A., et al. 2021, A&A, 656, A23
Halekas, J. S., Whittlesey, P., Larson, D. E., et al. 2022, ApJ, 936, 53
Hammond, C. M., Feldman, W. C., Mccomas, D. J., Phillips, J. L., & Forsyth, R. J. 1996, A&A, 316, 350
Horbury, T. S., O'Brien, H., Blazquez, I. C., et al. 2020, A&A, 642, A9
Huttunen, K. E. J., Bale, S. D., Phan, T. D., Davis, M., & Gosling, J. T. 2007, J. Geophys. Res.: Space Phys., 112, A01102
Karlsson, T., Heyner, D., Volwerk, M., et al. 2021, J. Geophys. Res.: Space Phys., 126, e2020JA028961
Khotyaintsev, Y. V., Graham, D. B., Vaivads, A., et al. 2021, A&A, 656, A19
Lin, R. P. 1990, Symp. Int. Astron. Union, 142, 467
Lin, N., Kellogg, P. J., MacDowall, R. J., et al. 1995, Geophys. Res. Lett., 22, 3417
MacDowall, R. J., Lin, N., Kellogg, P. J., et al. 2008, Langmuir Waves in Magnetic Holes: Source Mechanism and Consequences (AIP Publishing), 301
Madanian, H., Halekas, J. S., Mazelle, C. X., et al. 2020, J. Geophys. Res.: Space Phys., 125, e2019JA027198
Maksimovic, M., Zouganelis, I., Chaufray, J. Y., et al. 2005, J. Geophys. Res.: Space Phys., 110, A09104
Maksimovic, M., Bale, S. D., Chust, T., et al. 2020, Astron. Inst. Czech Acad. Sci., 17, 20
Malaspina, D. M., Cairns, I. H., & Ergun, R. E. 2011, Geophys. Res. Lett., 38, L13101
McComas, D. J., Bame, S. J., Feldman, W. C., Gosling, J. T., & Phillips, J. L. 1992, Geophys. Res. Lett., 19, 1291
Müller, D., St. Cyr, O. C., Zouganelis, I., et al. 2020, A&A, 642, A1
Owen, C. J., Abraham, J. B., Nicolaou, G., et al. 2022, Universe, 8, 509
Phillips, J. L., Gosling, J. T., McComas, D. J., et al. 1989, J. Geophys. Res.: Space Phys., 94, 6563
Pollock, C., Moore, T., Jacques, A., et al. 2016, Space Sci. Rev., 199, 331
Pulupa, M., Bale, S. D., Badman, S. T., et al. 2020, ApJS, 246, 49
Rasca, A. P., Farrell, W. M., Whittlesey, P. L., et al. 2022, ApJ, 935, 81
Robinson, P. A. 1992, Sol. Phys., 139, 147
Souček, J., Píša, D., Kolmasova, I., et al. 2021, A&A, 656, A26
Sperveslage, K., Neubauer, F. M., Baumgärtel, K., & Ness, N. F. 2000, Nonlinear Process. Geophys., 7, 191
Štverák, Š., Maksimovic, M., Trávníček, P. M., et al. 2009, J. Geophys. Res.: Space Phys., 114, A05104
Turner, J. M., Burlaga, L. F., Ness, N. F., & Lemaire, J. F. 1977, J. Geophys. Res., 82, 1921
Verscharen, D., Klein, K. G., & Maruca, B. A. 2019, Liv. Rev. Sol. Phys., 16, 5
Volwerk, M., Goetz, C., Plaschke, F., et al. 2020, Annal. Geophys., 38, 51
Vörös, Z., Varsani, A., Yordanova, E., et al. 2021, J. Geophys. Res.: Space Phys., 126, e2021JA029415
Winterhalter, D., Neugebauer, M., Goldstein, B. E., et al. 1994, J. Geophys. Res., 99, 23371
Yao, S. T., Wang, X. G., Shi, Q. Q., et al. 2017, J. Geophys. Res.: Space Phys., 122, 1990
Yao, S. T., Shi, Q. Q., Yao, Z. H., et al. 2019, Geophys. Res. Lett., 46, 523